

Nonlinear analysis of compact and thin-walled metallic structures including localized plasticity under contact conditions

Original

Nonlinear analysis of compact and thin-walled metallic structures including localized plasticity under contact conditions / Nagaraj, M. H.; Kaleel, I.; Carrera, E.; Petrolo, M.. - In: ENGINEERING STRUCTURES. - ISSN 0141-0296. - STAMPA. - 203:(2020). [10.1016/j.engstruct.2019.109819]

Availability:

This version is available at: 11583/2770756 since: 2019-12-02T17:45:06Z

Publisher:

Elsevier

Published

DOI:10.1016/j.engstruct.2019.109819

Terms of use:

This article is made available under terms and conditions as specified in the corresponding bibliographic description in the repository

Publisher copyright

Elsevier postprint/Author's Accepted Manuscript

© 2020. This manuscript version is made available under the CC-BY-NC-ND 4.0 license
<http://creativecommons.org/licenses/by-nc-nd/4.0/>. The final authenticated version is available online at:
<http://dx.doi.org/10.1016/j.engstruct.2019.109819>

(Article begins on next page)

Nonlinear analysis of compact and thin-walled metallic structures including localized plasticity under contact conditions

M.H. Nagaraj, I. Kaleel, E. Carrera, M. Petrolo
MUL² Group, Department of Mechanical and Aerospace Engineering
Politecnico di Torino, Corso Duca degli Abruzzi 24, 10129 Torino, Italy

Revised Version of ENGSTRUCT_2019_2646

Author for correspondence:

E. Carrera, Professor of Aerospace Structures and Aeroelasticity,
MUL² Group, Department of Mechanical and Aerospace Engineering,
Politecnico di Torino,
Corso Duca degli Abruzzi 24,
10129 Torino, Italy,
tel: +39 011 090 6836,
fax: +39 011 090 6899,
e-mail: erasmo.carrera@polito.it

Abstract

This work presents the numerical analysis of elastoplastic contact problems of compact and thin-walled metallic structures. The emphasis is on the use of higher-order 1D elements with pure displacement variables and based on the Carrera Unified Formulation (CUF) to capture localized effects and cross-sectional distortions. Contact interactions are normal and frictionless via a node-to-node contact algorithm with the penalty approach for contact enforcement. The analysis considers the material nonlinearity via the von Mises constitutive law. Numerical assessments compare the CUF solutions with 3D finite element analysis concerning the solution quality, computational size, and analysis time. The results show the ability of 1D CUF models of accurately evaluating localized deformations and plasticity. The CUF results are in good agreement with reference 3D finite element solutions, and require an order of magnitude fewer degrees of freedom and analysis time, making them computationally efficient.

Keywords: Node-to-Node contact, CUF, elastoplastic contact

1 Introduction

The analysis of systems involving multiple bodies in physical contact is a common engineering problem leading to nonlinearities due to the changing boundary conditions resulting from contact interactions. The presence of material and geometrical nonlinearities can further add to the complexity of the problem, making it difficult and costly to solve. An example of such a nonlinear problem is the elastoplastic contact that may arise in many practical applications such as the sheet metal forming, indentation tests, and meshing gears.

The elastoplastic contact analysis can use various approaches, and a brief overview of them follows. An analytical solution to the indentation of a rigid sphere into a rigid-perfectly plastic half-space dates back to the 40s [1], while a theoretical model for the indentation of an elastoplastic half-space is in [2]. A semi-analytical approach to the 3D analysis of elastoplastic contact with hardening behavior is the aim of [3]. The flexibility of the finite element (FE) method makes it a prevalent numerical tool for nonlinear structural analysis, and a large body of work dealing with FE of elastoplastic contact is available in the literature. An example of early works involving FE is the analysis of flat punch indentation [4]. Other works include the indentation of an elastoplastic substrate by a periodic array of elastic strip punches [5], and the indentation of layered media [6, 7]. Other numerical approaches applied to the case of elastoplastic contact include the Boundary Element Method (BEM) [8, 9], and a combination of FE and BEM [10]. Alternative approaches to tackle 3D elastoplastic problems are in [11] and [12].

Structural constraints often require a 3D numerical analysis, potentially leading to high computational costs. Because of this, a lot of effort focused on the development of refined beam theories to obtain accurate solutions at reduced computational costs. Approaches to refined beam modeling include the Generalised Beam Theory [13] and the Variational Asymptotic Method [14]. Wriggers et al. developed specific contact algorithms for beam models for the case of beams in contact [15–18]. The current work uses refined beam models based on Carrera Unified Formulation (CUF)[19] to tackle elastoplastic contact problems as accurately as 3D FE without the corresponding computational costs. Recently, CUF proved to be valid for several computationally expensive problems such as nonlinear structural problems taking into account geometrical nonlinearities [20], material nonlinearities [21, 22], and multi-scale analysis of composite structures [23, 24], offering multi-fold reductions in computational times and memory requirements.

The current work focuses on the use of refined 1D CUF models to solve problems of elastoplastic contact for metallic structures. The paper has the following sections: Section 2 describes the development of 1D structural theories in CUF. Section 3 shows contact mechanics and its implementation in the form of a node-to-node formulation. Section 4 presents some numerical assessments followed by conclusions in Section 5.

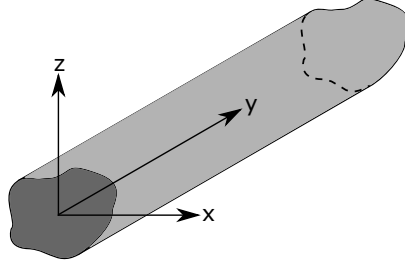


Figure 1: Reference system

2 Structural theories and FE formulation

Considering a beam segment aligned along the y -axis, as shown in Fig. 1, the displacement field as defined by CUF is

$$\mathbf{u}(x, y, z) = F_\tau(x, z)\mathbf{u}_\tau(y), \tau = 1, 2, \dots, M \quad (1)$$

where the expansion function F_τ describes the cross-section kinematics and $\mathbf{u}_\tau(y)$ are the generalized displacements. The number of terms in the expansion function is M . The choice of F_τ and M defines the structural theory used in the analysis. The present work considers the Lagrange-expansion (LE) class to define the cross-sectional displacement field. Such expansion results in purely displacement degrees of freedom (DOF). As an example, the displacement field of the 9-node quadratic element (L9) is

$$\begin{aligned} u_x &= \sum_{\tau=1}^9 F_\tau(x, z)u_{x\tau}(y) \\ u_y &= \sum_{\tau=1}^9 F_\tau(x, z)u_{y\tau}(y) \\ u_z &= \sum_{\tau=1}^9 F_\tau(x, z)u_{z\tau}(y) \end{aligned} \quad (2)$$

where $u_{x\tau}$, $u_{y\tau}$, and $u_{z\tau}$ are the DOF. Further details on the use of Lagrange polynomials as a class of expansion functions in CUF are in [25].

The stress and strain vectors are

$$\begin{aligned} \boldsymbol{\sigma} &= \{\sigma_{xx}, \sigma_{yy}, \sigma_{zz}, \sigma_{xy}, \sigma_{xz}, \sigma_{yz}\}^T \\ \boldsymbol{\varepsilon} &= \{\varepsilon_{xx}, \varepsilon_{yy}, \varepsilon_{zz}, \varepsilon_{xy}, \varepsilon_{xz}, \varepsilon_{yz}\}^T \end{aligned} \quad (3)$$

The linear strain-displacement relation is

$$\boldsymbol{\varepsilon} = \mathbf{D}\mathbf{u} \quad (4)$$

where \mathbf{D} is

$$\mathbf{D} = \begin{bmatrix} \frac{\partial}{\partial x} & 0 & 0 \\ 0 & \frac{\partial}{\partial y} & 0 \\ 0 & 0 & \frac{\partial}{\partial z} \\ \frac{\partial}{\partial y} & \frac{\partial}{\partial x} & 0 \\ \frac{\partial}{\partial z} & 0 & \frac{\partial}{\partial x} \\ 0 & \frac{\partial}{\partial z} & \frac{\partial}{\partial y} \end{bmatrix}$$

The stress-strain relationship, considering the physical nonlinearity, is

$$\boldsymbol{\sigma} = \mathbf{C}^{cep} \boldsymbol{\varepsilon} \quad (5)$$

where \mathbf{C}^{cep} is the consistent elastoplastic material matrix. Further details on the theory and implementation of the von Mises plasticity model in CUF are in [21].

The structure has 1D elements along the longitudinal axis using nodal interpolation functions N_i , leading to the following displacement field:

$$\mathbf{u}(x, y, z) = F_\tau(x, z) N_i(y) \mathbf{u}_{\tau i} \quad (6)$$

Via the principle of virtual displacements,

$$\delta L_{int} = \delta L_{ext} \quad (7)$$

where δL_{int} is the virtual variation of the internal strain energy, defined as

$$\delta L_{int} = \int_V \delta \boldsymbol{\varepsilon}^T \boldsymbol{\sigma} dV \quad (8)$$

L_{ext} is the work due to external loading

$$L_{ext} = F_s N_j \delta \mathbf{u}_{sj}^T \mathbf{P} \quad (9)$$

where \mathbf{P} is the external force vector. Combining Eqs. (5), (6) and (8) leads to

$$\delta L_{int} = \delta \mathbf{u}_{sj}^T \mathbf{k}_{ij\tau s}^{tan} \mathbf{u}_{\tau i} \quad (10)$$

where,

$$\mathbf{k}_{ij\tau s}^{tan} = \int_l \int_A \mathbf{D}^T (N_i(y) F_\tau(x, z)) \mathbf{C}^{cep} \mathbf{D} (N_j(y) F_s(x, z)) dA dl \quad (11)$$

The term $\mathbf{k}_{ij\tau s}^{tan}$ is a 3×3 matrix, termed the Fundamental Nucleus (FN), and whose form remains invariant for any expansion type and order. The element stiffness matrix stems from the assembly of the FN for all

combinations of i, j, τ , and s . Further explanations on the role of the fundamental nucleus in CUF are in [19].

3 Contact Mechanics

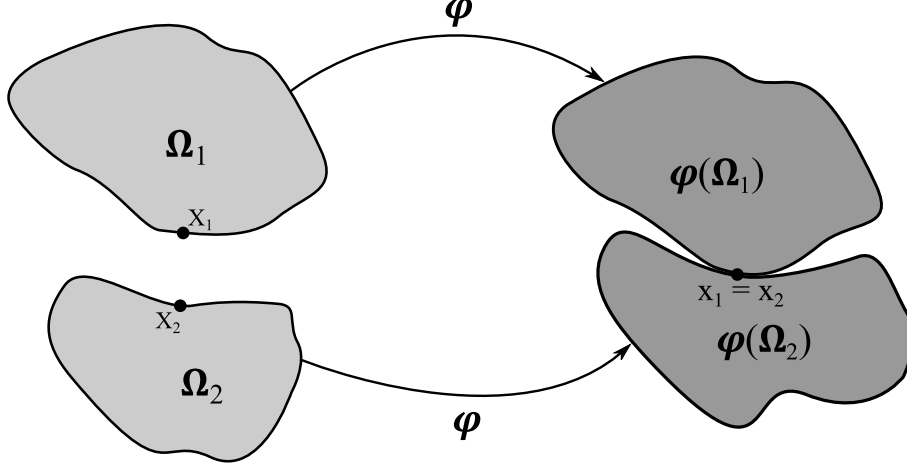


Figure 2: Reference and current configuration of two distinct bodies coming into contact

Let us consider two distinct bodies $\Omega_i, i = 1, 2$, as shown in Fig. 2. Two distinct points X_1 and X_2 , initially on the boundary of the respective bodies, come into contact with each other due to the applied deformation φ . The position of the points X_i in the deformed configuration is

$$\mathbf{x}_i = \mathbf{X}_i + \mathbf{u}_i; \quad i = 1, 2 \quad (12)$$

where \mathbf{u}_i is the displacement of the reference point X_i . When contact occurs between the two bodies, the two points occupy the same physical space, i.e., $\mathbf{x}_1 = \mathbf{x}_2$. The non-penetration condition between the bodies leads to the following form of the gap function g_N :

$$g_N = (\mathbf{u}_2 - \mathbf{u}_1) \cdot \mathbf{n}_1 + g_{init} \geq 0 \quad (13)$$

where \mathbf{n}_1 is the vector normal to Ω_1 , and g_{init} , the initial gap between the two bodies,

$$g_{init} = (\mathbf{X}_2 - \mathbf{X}_1) \cdot \mathbf{n}_1 \quad (14)$$

The variational form, considering contact, is

$$\delta L_{int} \geq \delta L_{ext} + \delta L_c \quad (15)$$

where δL_c is the variation of the work due to contact. Treating the contact constraint using a penalty

approach, the work due to contact takes the form

$$L_c = \frac{1}{2} \int_{\partial\Omega_c} \epsilon_N g_N^2 dA \quad (16)$$

where $\partial\Omega_c$ is the contact surface, and ϵ_N is the penalty parameter for normal contact. The virtual variation is then given by

$$\delta L_c = \int_{\partial\Omega_c} \epsilon_N g_N \delta g_N dA \quad (17)$$

In the node-to-node formulation, the contact constraints act at the nodal level. Via the penalty approach, the global equilibrium equation becomes

$$[\mathbf{K}^{tan} + \mathbf{K}^p] \mathbf{U} = \bar{\mathbf{F}} \quad (18)$$

solved incrementally using the Newton method. \mathbf{K}^p is the global penalty stiffness matrix formed by the assembly of the penalty stiffness terms for a given node pair,

$$\mathbf{k}_i^p = \epsilon_N \mathbf{n}_i^T \mathbf{n}_i \quad (19)$$

where $\mathbf{n}_i = \{n_x, n_y, n_z\}$ is the unit normal vector between the node pair i . The nodal contact forces for the node pair is

$$\mathbf{F}_i^c = \epsilon_N g_N \mathbf{n}_i \quad (20)$$

The sum of the contact force and the external force vectors represents the right-hand side of Eq. 18,

$$\bar{\mathbf{F}} = \mathbf{F}^c + \mathbf{F}_{ext} \quad (21)$$

Figure 3 shows a schematic description of the solution. CUF serves as the generator of the arrays consistently with the structural theory adopted. A classic nonlinear solver handles the nonlinearities.

4 Numerical Examples

4.1 Indentation of an elastoplastic block

The current example considers the case of a rectangular elastoplastic block subjected to indentation by a rigid flat indenter, see Fig. 4. The dimension along y is 0.1 m. The bottom surface of the block is clamped, and the top surface of the indenter has a prescribed downward displacement, $u_z = 1.0$ mm. The elastoplastic block is isotropic, with a Young Modulus $E = 70$ GPa, Poisson ratio $\nu = 0.3$, and an initial yield stress $\sigma_y = 100.0$ MPa. The analysis assumes perfect plasticity resulting in a hardening modulus $H = 0$. The numerical results

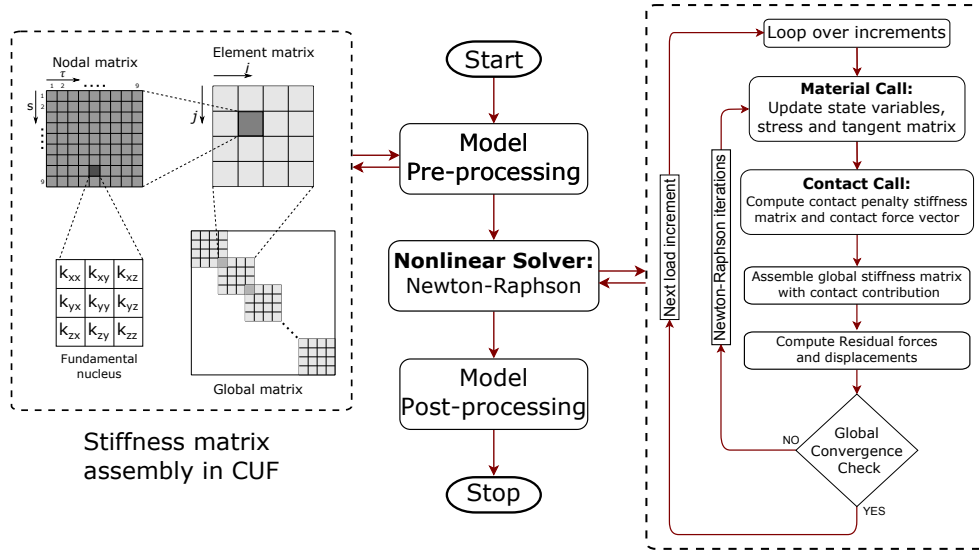


Figure 3: Flowchart of the solution scheme within CUF

stem from 1D CUF models and 3D FE in ABAQUS via eight-node brick elements (C3D8R).

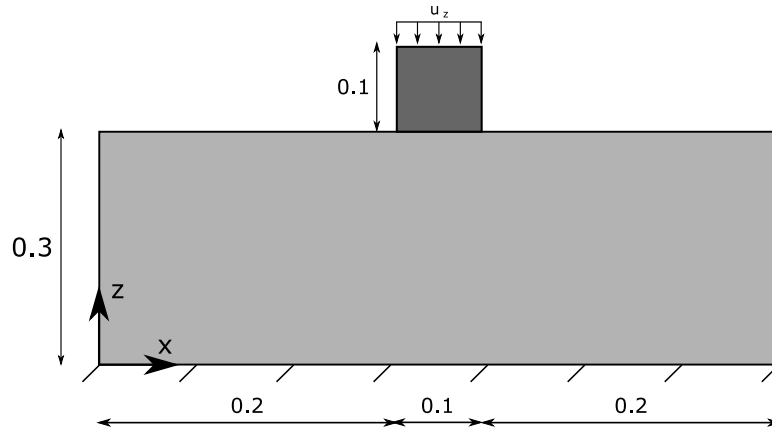


Figure 4: A schematic representation of the elastoplastic rectangular block subjected to indentation, all units in m

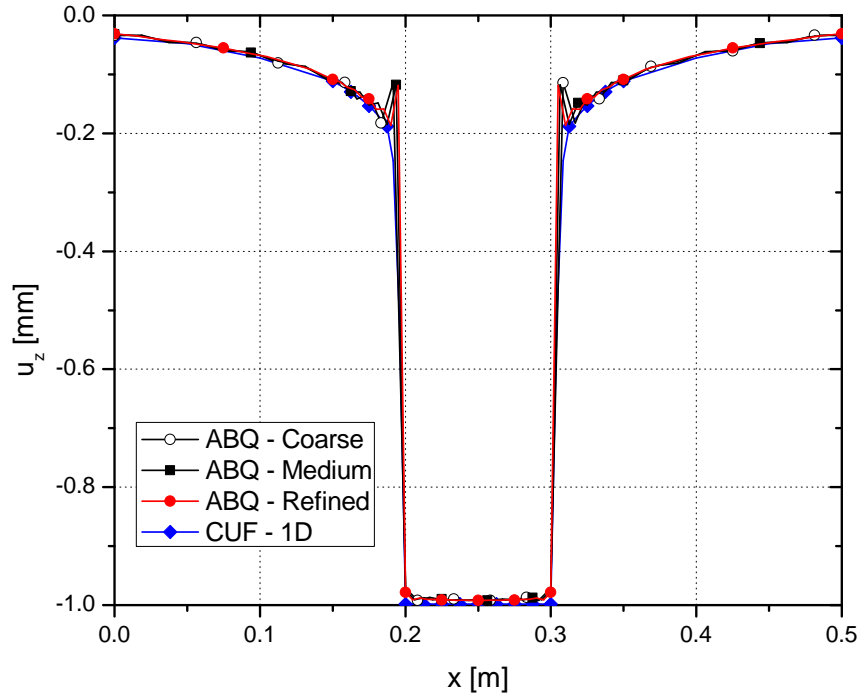
Table 1 summarizes the model information for the various numerical analyses. The vertical displacement u_z along the line joining the points $[0.0, 0.05, 0.3]$ and $[0.5, 0.05, 0.3]$, i.e., the longitudinal axis of the top surface of the rectangular block, is in Fig. 5. The normal stress, σ_{zz} , along the same line is in Fig. 6. The distribution of the equivalent plastic strains in the contact region is in Fig. 7. Table 2 summarizes some results at the edge of the contact region, i.e., the point $[0.2, 0.05, 0.3]$.

The numerical results suggest that

1. The numerical assessment verifies the capability of CUF models in handling problems involving coupled nonlinearities, i.e., elastoplastic contact.
2. The 1D CUF results are in good agreement with those obtained by 3D FE. There is a perfect match concerning the transverse displacement distributions. On the other hand, some differences are observable in the stress and strain fields. Such differences are at the edge of the indenter and are particularly

Table 1: Model information for the finite element analysis of the elastoplastic block subjected to indentation

Model	Discretization of the elastoplastic block	DOF	Time (s)
ABQ - Coarse	10,560 C3D8R	36,777	132
ABQ - Medium	21,504 C3D8R	72,471	382
ABQ - Refined	40,800 C3D8R	134,505	1161
CUF - 1D	108L9 - 1B4	5,772	210

**Figure 5:** Vertical displacement u_z along the top surface of the rectangular block**Table 2:** Numerical results at the edge of the contact region of the block [0.2, 0.05, 0.3]

Model	σ_{zz} [MPa]	Eq. plastic strain [-]
ABQ - Coarse	-185.2	$4.04 \cdot 10^{-2}$
ABQ - Medium	-193.2	$5.21 \cdot 10^{-2}$
ABQ - Fine	-198.05	$6.38 \cdot 10^{-2}$
CUF - 1D	-296.1	$6.58 \cdot 10^{-2}$

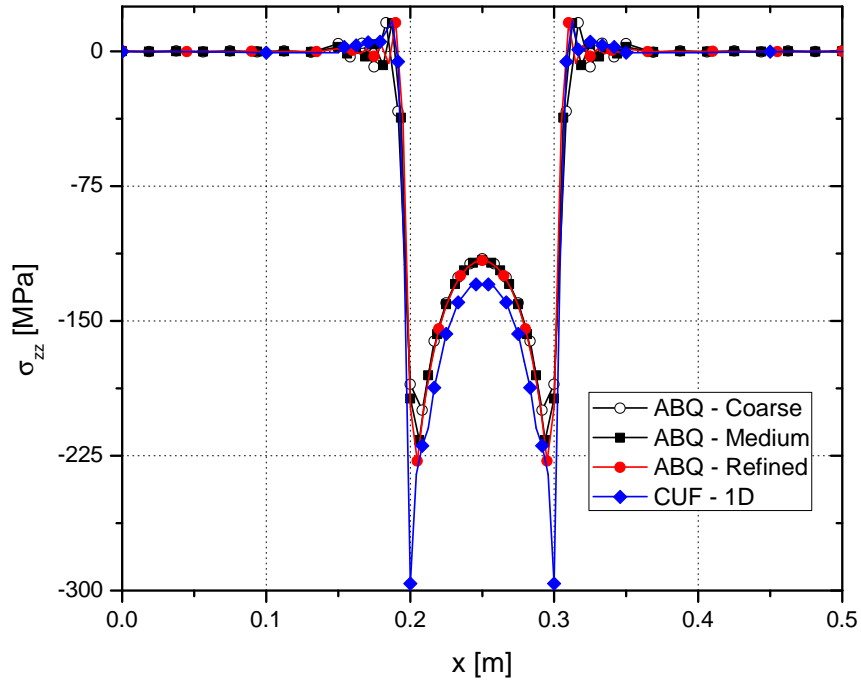


Figure 6: Normal stress σ_{zz} along the top surface of the rectangular block

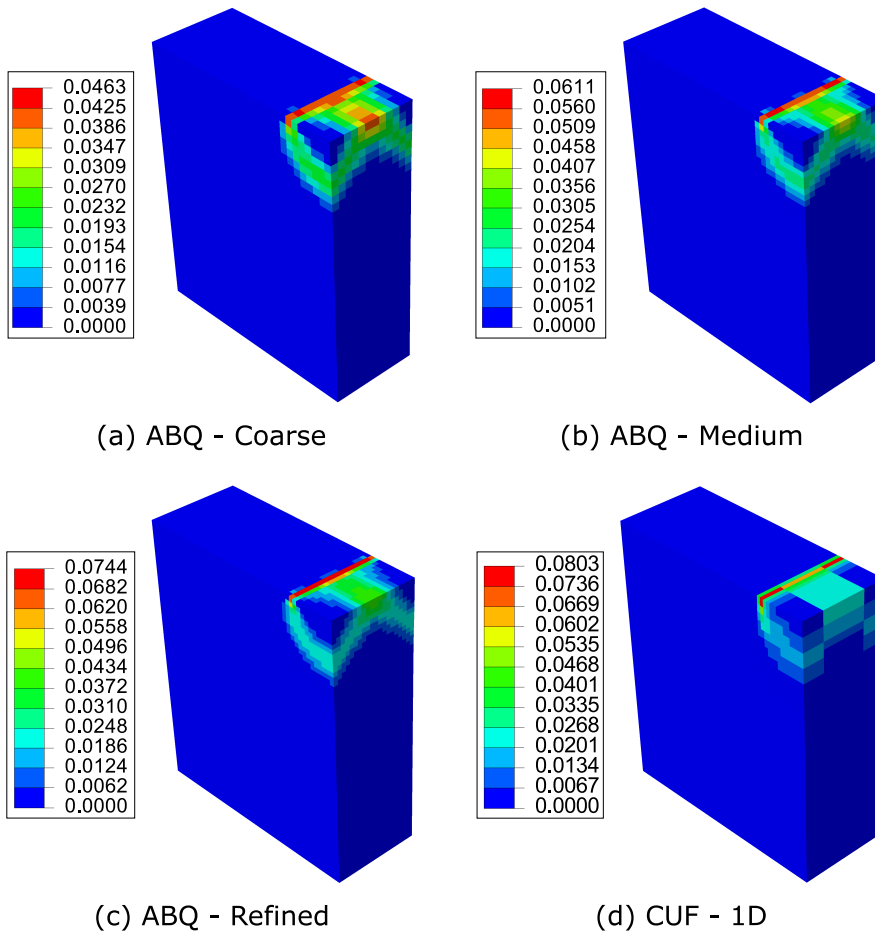


Figure 7: Plastic strain in the contact region of the rectangular block

significant for the stress. In both cases, the refinement process of the 3D models tends to the CUF. Such behavior is consistent with the findings related to composite structures in [26].

3. The number of DOF required by the CUF model is some 7 to 30 times smaller than 3D FE depending on the mesh density. However, the reduction in the computational time of the CUF model is not consistent with the DOF count. Such an inconsistency stems from the contact algorithm implemented not having the same optimized capabilities of the one in ABAQUS.
4. Although the CUF implementation is 1D, 3D fields are available and accurate.

4.2 Three-point bending of compact and thin-walled section beams

The current example comprises of two structural configurations, namely, a compact square beam and a thin-walled square-section tube subjected to a 3-point bending test as in [27]. Supports are two rollers, and a central one applies the load, i.e., a vertical downward deflection, $u_z = -0.75$ mm. Figure 8 shows the geometry of the structure. The compact cross-section has an edge length of 10 mm, and all the other parameters are as for the thin-walled case. The material properties are as follows: $E = 68$ GPa, $\nu = 0.33$, and yield stress 29 MPa. The hardening is piece-wise linear isotropic and based on the stress-plastic strain plot given in Fig. 9. As in the previous section, results stem from 1D CUF and 3D FE from ABAQUS via eight-node and twenty-node brick elements (C3D8R and C3D20R). A summary of the various numerical models are in Tables 3 and 4.

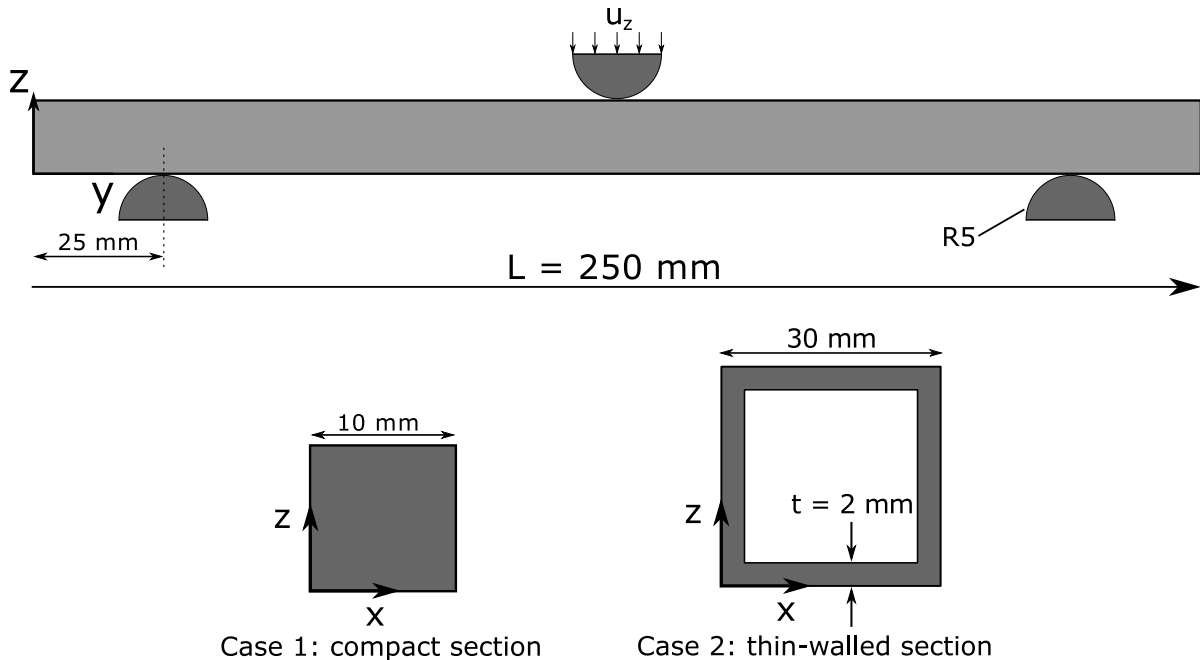


Figure 8: A schematic representation of three-point bending cases

Concerning the compact section, the axial stress, σ_{yy} , along the axis of the beam at its top surface is in Fig. 10 and the equivalent plastic strain in Fig. 11. The distribution of the normal strain component, ε_{zz} , is in Fig.

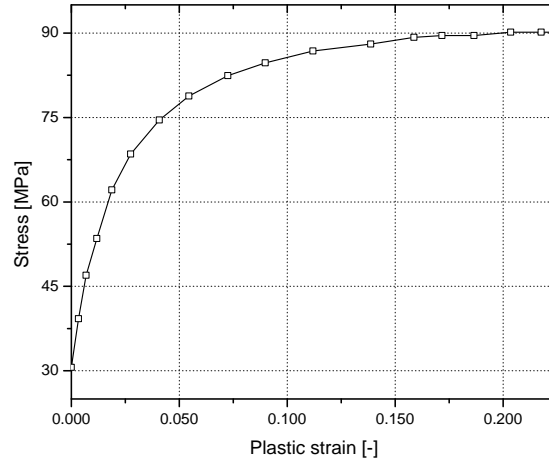


Figure 9: Piece-wise linear hardening curve of the material used in the square tube

Table 3: Model information for the finite element analyses of the compact-section beam under three-point bending

Model	Discretization of the beam	DOF	Time (s)
ABQ - Coarse	3,024 C3D8R	12,495	40
ABQ - Refined	25,056 C3D8R	88,725	531
CUF - 1D (4L9)	10 B4 - 4 L9	2,325	73
CUF - 1D (16L9)	10 B4 - 16 L9	7,533	226

Table 4: Model information for the finite element analyses of the thin-walled square-section tube under three-point bending

Model	Discretization of the square tube	DOF	Time (hh:mm:ss)
ABQ - Coarse	3,344 C3D8R	20,328	00:08:43
ABQ - Medium	76,464 C3D8R	307,152	00:57:00
ABQ - Refined	129,600 C3D8R	456,120	01:44:35
ABQ - Quadratic	19,008 C3D20R	315,360	00:50:45
CUF - 1D (20L9)	22 B4 - 20 L9	24,120	00:17:52
CUF - 1D (28L9)	22 B4 - 28 L9	33,768	00:26:04

12 and the equivalent plastic strains is in Fig. 13. Numerical results at the center of the contact region, $[0.005, 0.125, 0.01]$, are in Table 5.

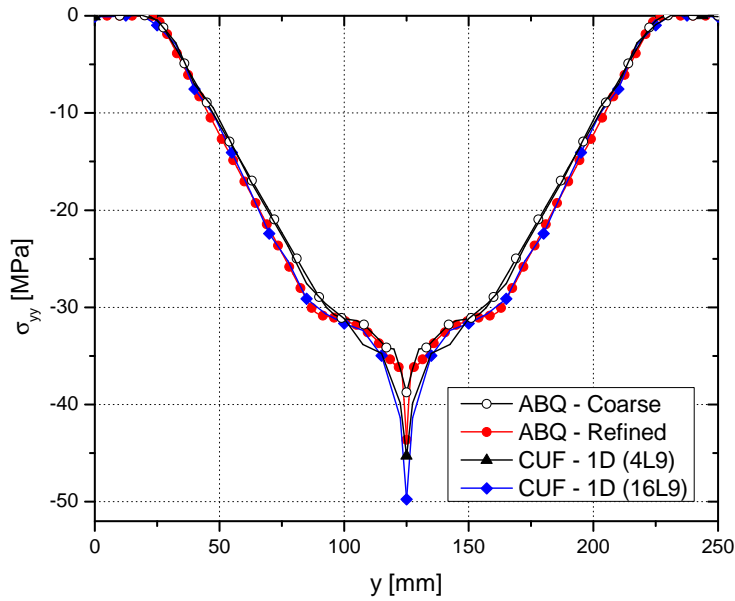


Figure 10: Axial stress σ_{yy} along the top surface of the compact beam

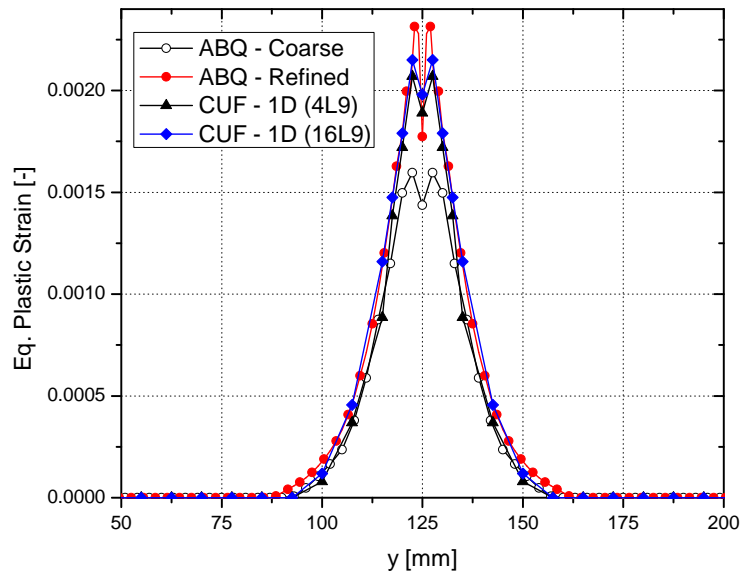


Figure 11: Equivalent plastic strain along the top surface of the compact beam

For the thin-walled case, the discretization used for the ABQ - Quadratic and CUF 1D (28L9) analyses are in Fig. 14. The vertical deflection, u_z , at the top of the beam and along its longitudinal axis is in Fig. 15, the axial stress, σ_{yy} , and the equivalent plastic strains along the same line are in Fig. 16 and Fig. 17, respectively. The 3D equivalent plastic strain distribution of the tube is in Fig. 18. The numerical results at the center of the contact region, i.e., $[0.015, 0.125, 0.030]$, are in Table 6.

The numerical results show that

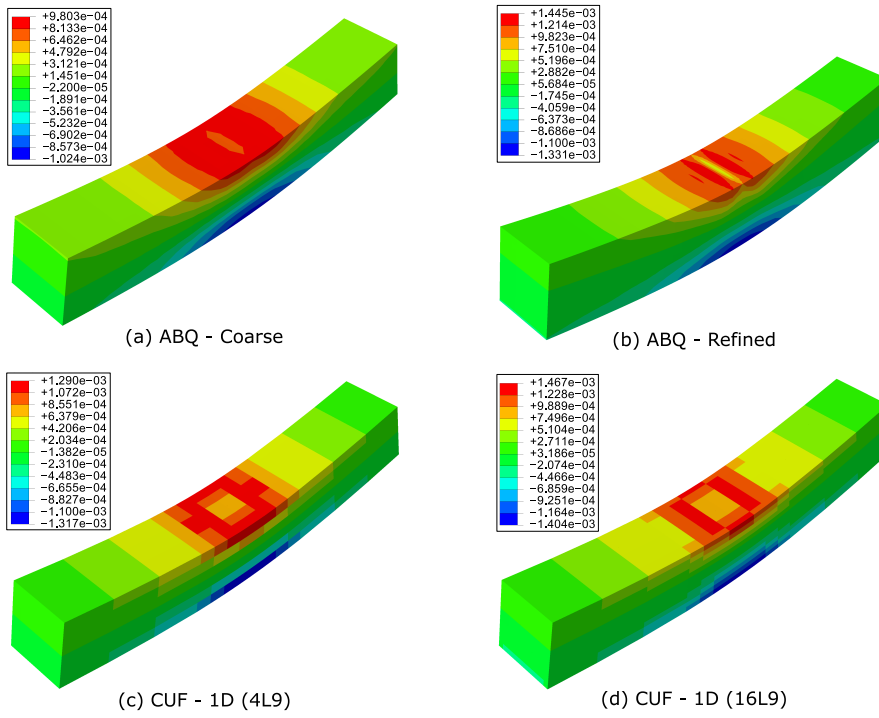


Figure 12: Distribution of the elastic strain component ε_{zz} at the contact region

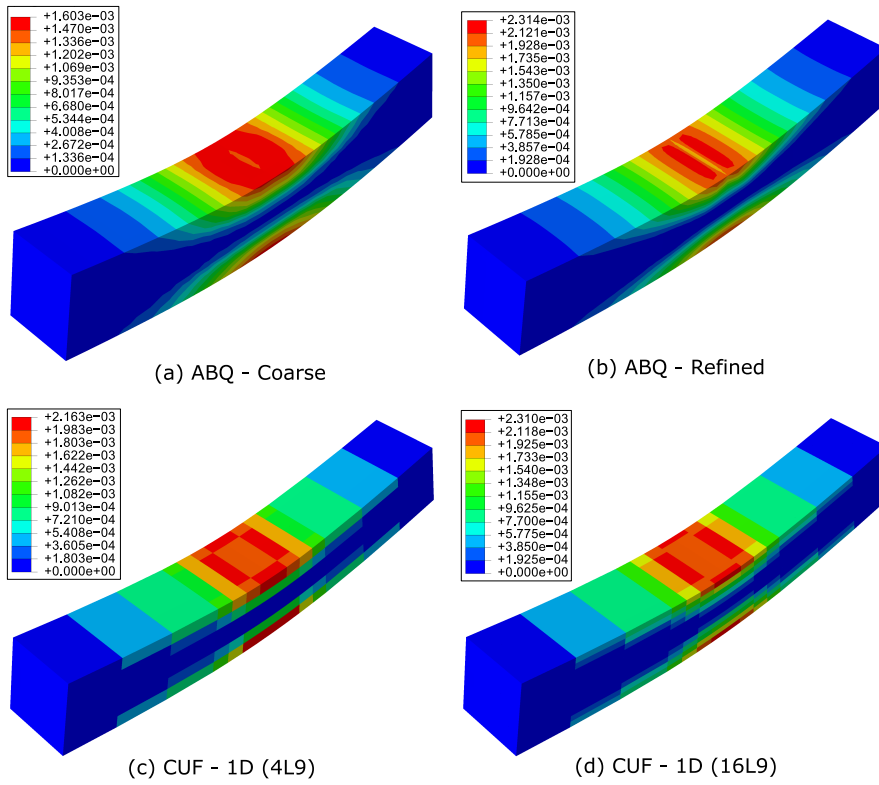


Figure 13: Distribution of the equivalent plastic strain at the contact region

Table 5: Numerical results at the center of the contact region for the compact section

Model	σ_{yy} [MPa]	Eq. plastic strain [-]
ABQ - Coarse	-38.75	$1.43 \cdot 10^{-3}$
ABQ - Refined	-43.63	$1.77 \cdot 10^{-3}$
CUF - 1D (4L9)	-45.30	$1.89 \cdot 10^{-3}$
CUF - 1D (16L9)	-49.75	$1.98 \cdot 10^{-3}$

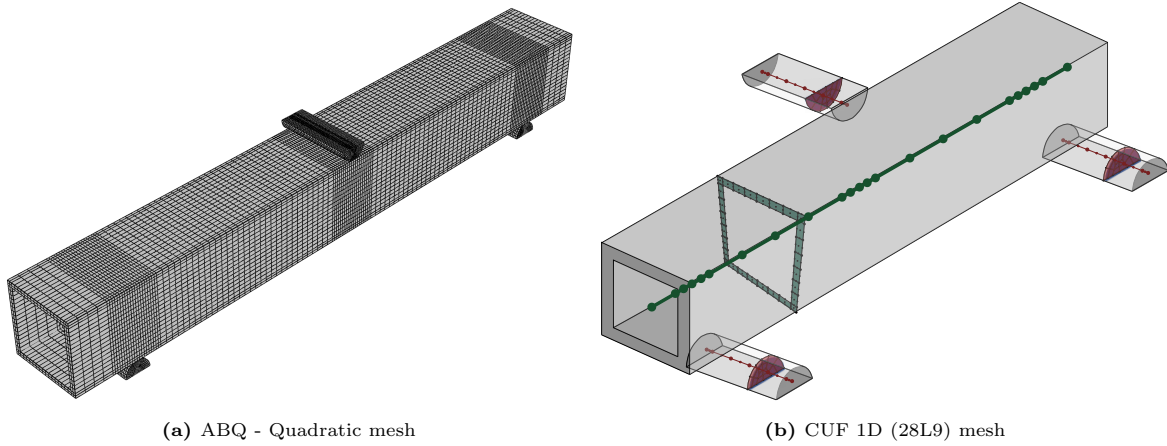


Figure 14: Discretization of the structure for the thin-walled case; (a) ABQ - Quadratic mesh, (b) CUF 1D (28L9) mesh

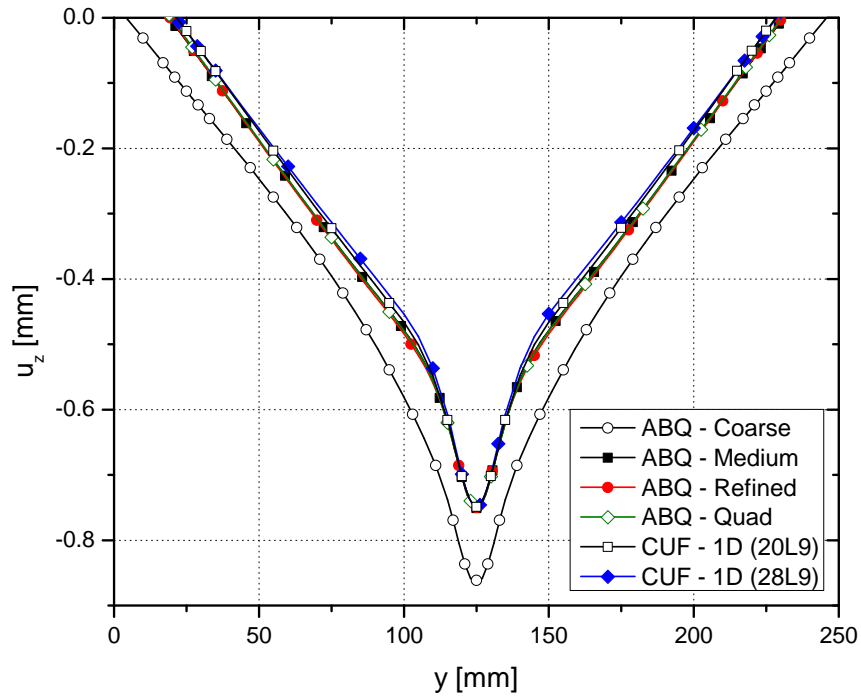


Figure 15: Vertical deflection u_z along the axis of the thin-walled tube subjected to three-point bending

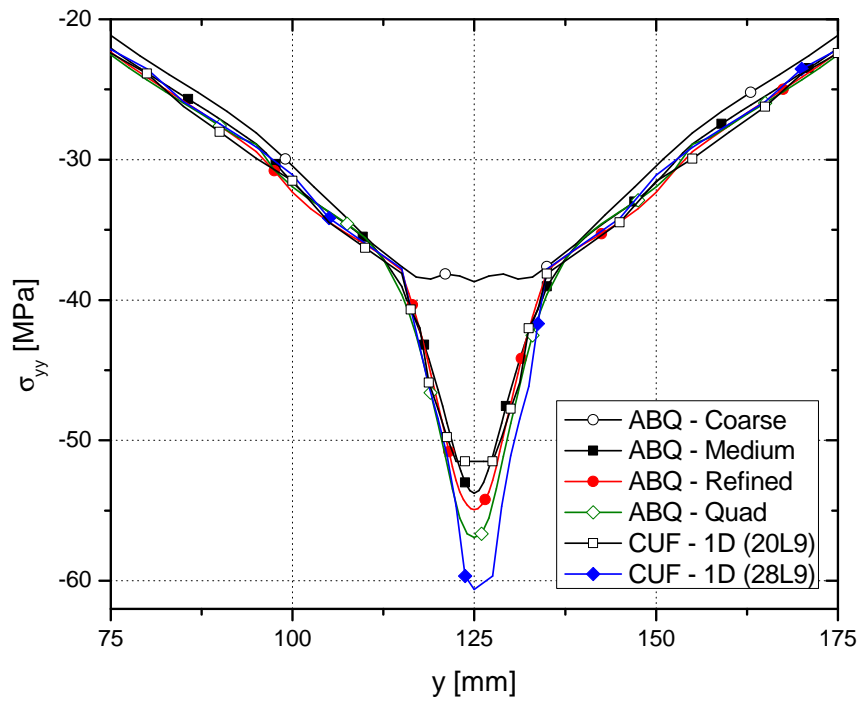


Figure 16: Axial stress σ_{yy} along the axis of thin-walled tube subjected to three-point bending

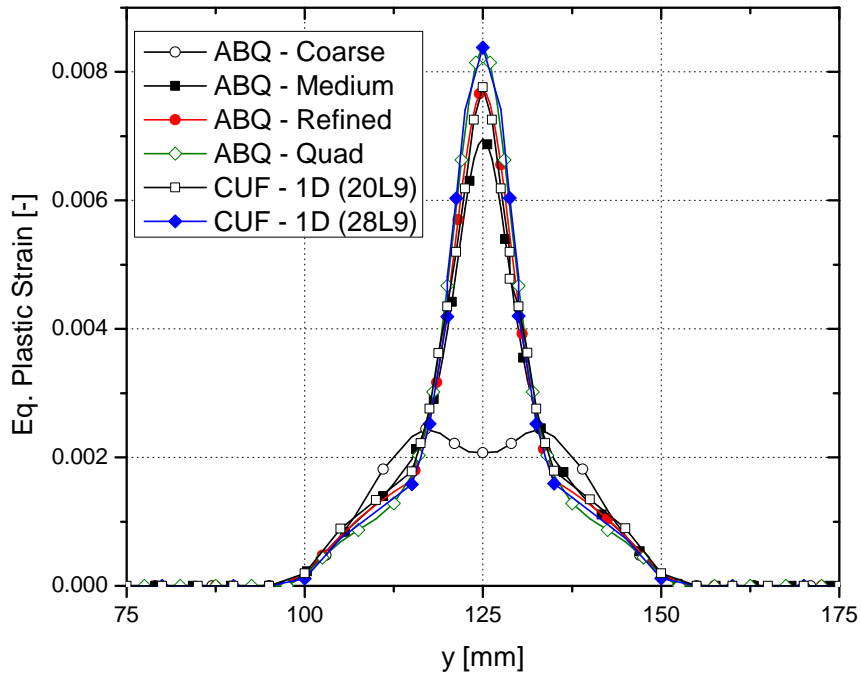


Figure 17: Equivalent plastic strain along the axis of the thin-walled tube subjected to three-point bending

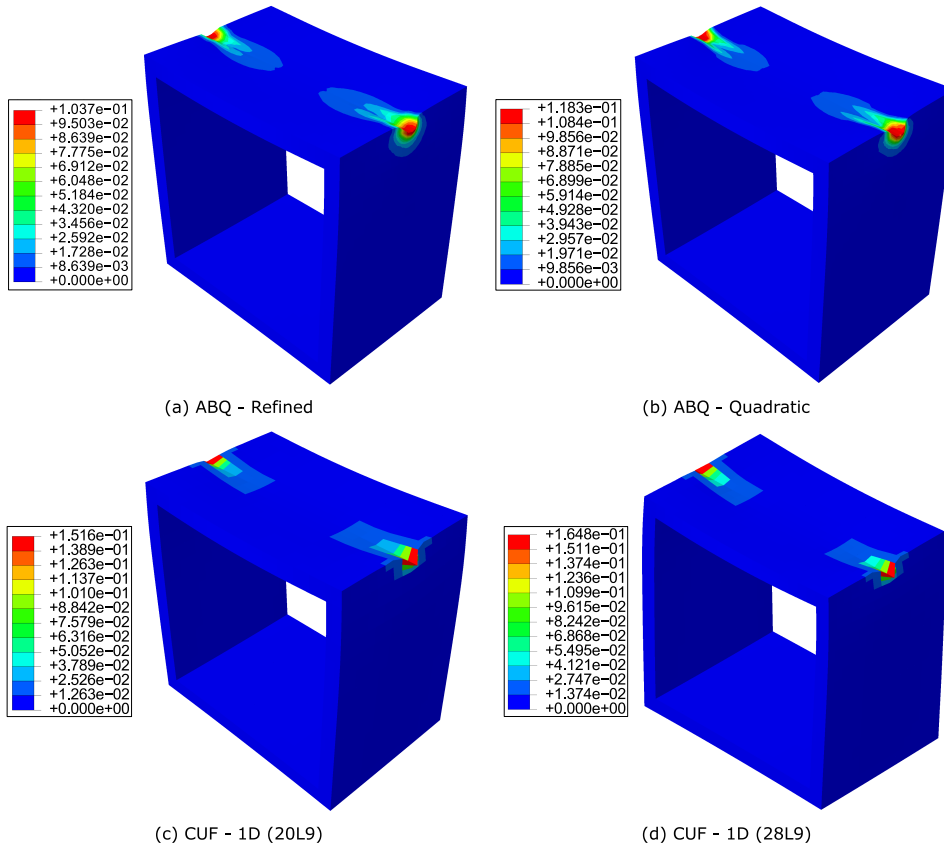


Figure 18: Equivalent plastic strain distribution at the midspan of the thin-walled tube subjected to three-point bending

Table 6: Numerical results at the centre of the contact region for the thin-walled tube subjected to three-point bending

Model	σ_{yy} [MPa]	Eq. plastic strain [-]
ABQ - Coarse	-38.68	$2.07 \cdot 10^{-3}$
ABQ - Medium	-53.76	$6.95 \cdot 10^{-3}$
ABQ - Fine	-54.93	$7.91 \cdot 10^{-3}$
ABQ - Quad	-56.91	$8.40 \cdot 10^{-3}$
CUF - 1D (20L9)	-51.50	$7.76 \cdot 10^{-3}$
CUF - 1D (28L9)	-60.60	$8.38 \cdot 10^{-3}$

1. In general terms, the present numerical assessments confirm the findings of the previous case concerning the accuracy and computational costs.
2. The advantages of the present 1D formulation are evident in the case of thin-walled structures. In fact, with 10% of 3D FE DOF, the 1D model provides all local stress fields and distortions, including local plasticity. For the compact cross-section, the advantages are still in place but less remarkable.
3. The main reason for the efficiency of the 1D model for the thin-walled case stems from the ability to independently refine the cross-section discretization while keeping the beam discretization constant. In other words, there are no element aspect ratio constraints as in the 3D case.
4. The coarsening of the mesh can lead to significant degradations of the results due to poor contact interactions and load transfer.

4.3 Cantilever beams in contact

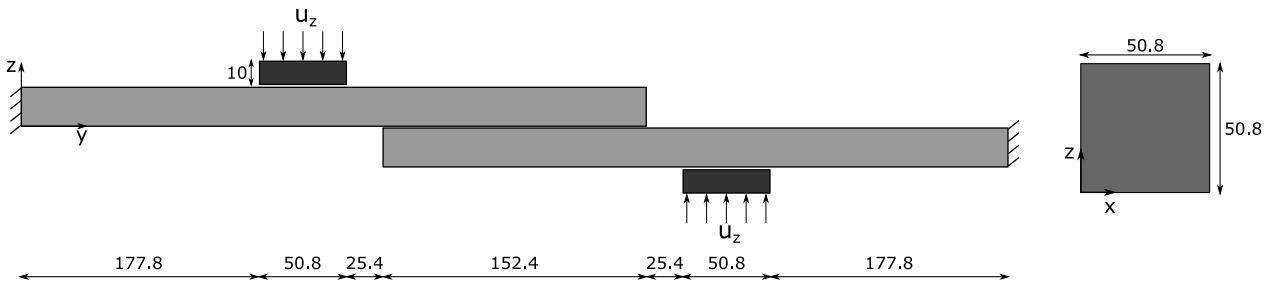


Figure 19: A schematic representation of two cantilever beams in contact, all units in mm

The current example considers two cantilever beams in contact with each other, as shown schematically in Fig. 19. The structural configuration comes from [28] with the load being applied via two rigid indenters, $u_z = 2.50$ mm per indenter. The material characteristics are the following: $E = 200$ GPa, $\nu = 0.30$, yield strength 242.2 MPa, and hardening modulus $H = 0$. A summary of the FE discretizations are in Table 7. The axial stress σ_{yy} along the longitudinal axis of the top surface of the cantilever beam is in Fig. 20. The distribution of the equivalent plastic strains in the beam, around the indented region, is shown in Fig. 21. Table 8 summarizes some numerical results at specific points of the cantilever beam. The numerical results suggest that

1. As in previous cases, the present 1D formulation can detect the 3D fields accurately.
2. The accuracy of the proposed formulation is comparable to quadratic 3D FE.
3. Concerning the DOF, the 1D model requires 20% of the quadratic 3D model's DOF.

Table 7: Model information for the finite element analyses of two cantilever beams in contact

Model	Discretization of each cantilever beam	DOF	Time [s]
ABQ - Coarse	4,224 C3D8R	32,562	234
ABQ - Medium	8,500 C3D8R	62,436	406
ABQ - Refined	15,552 C3D8R	110,526	712
ABQ - Quadratic	1,584 C3D20R	48,846	465
CUF - 1D	10 B4 - 16 L9	15,066	318

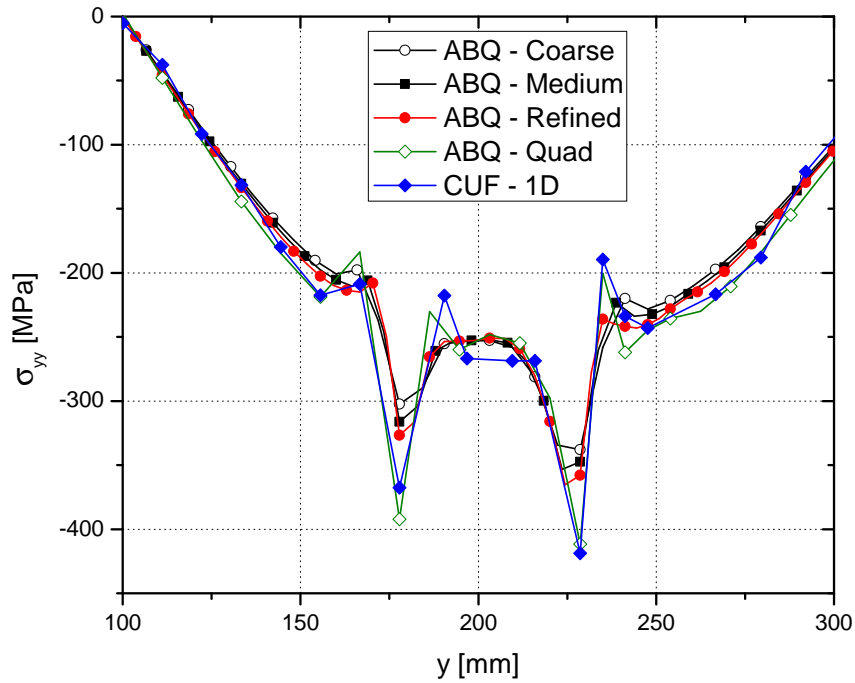


Figure 20: Axial stress along the top surface of the cantilever beam

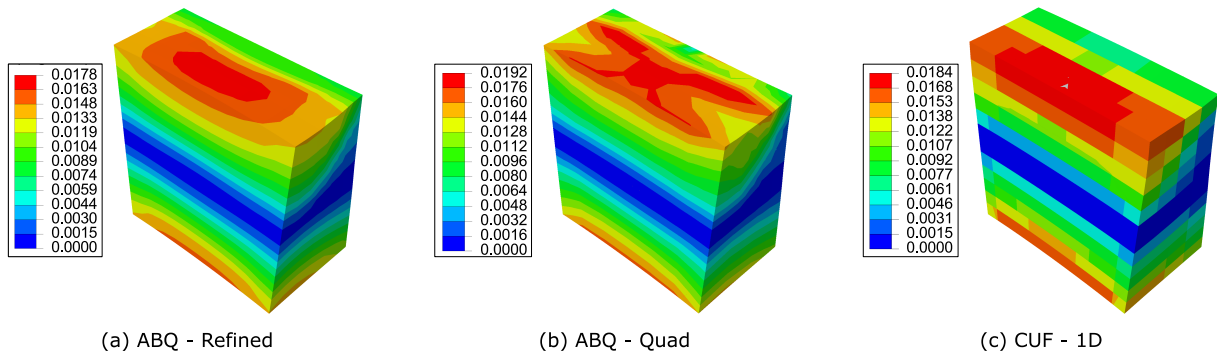


Figure 21: Distribution of the equivalent plastic strains at the center of the contact region between the beam and the first indenter

Table 8: Numerical results at specific points on the top surface of the cantilever beam

Model	σ_{yy} [MPa] y = 177.8 mm	σ_{yy} [MPa] y = 228.6 mm
ABQ - Coarse	-302.3	-338.0
ABQ - Medium	-316.1	-347.4
ABQ - Fine	-326.7	-357.9
ABQ - Quad	-392.3	-411.7
CUF - 1D	-367.6	-418.8

5 Conclusion

The focus of the current work is on the elastoplastic contact analysis of compact and thin-walled metallic structures. The aim is to diminish the computational overheads of nonlinear analyses without accuracy degradations. The numerical framework of this paper adopts the Carrera Unified Formulation (CUF) as the structural theory generator. More precisely, this paper uses CUF 1D models based on Lagrange expansions along the cross-section with pure displacement as the primary variables. The result verification exploits 3D FE models from ABAQUS. The analysis considers three structural configurations, namely, 3D block indentations, three-point bending of compact and thin-walled structures, and contact between two beams. The numerical results show that

1. The present framework succeeds in providing results as accurate as of the 3D FE.
2. The accuracy of the 1D models does not depend on the problem features such as the presence of local effects, severe distortions, or 3D stress fields.
3. Overall, the proposed 1D models are comparable to quadratic 3D FE concerning accuracy.
4. The reduction in computational costs originates from the decrease of DOF - some 10% -20% as compared to 3D FE. Further improvements in the contact algorithm implementation can drastically reduce the analysis time as well.

Future works should consider the implementation of surface-based contact algorithms, and the extension of the framework to the impact analysis of composite structures.

Acknowledgments

This research work has been carried out within the project ICONIC (Improving the Crashworthiness of Composite Transportation Structures), funded by the European Union Horizon 2020 Research and Innovation program under the Marie Skłodowska-Curie Grant agreement No. 721256, and the project FULLCOMP (Fully integrated analysis, design, manufacturing and health-monitoring of composite structures), funded by the European Union Horizon 2020 Research and Innovation program under the Marie Skłodowska-Curie Grant agreement No. 642121.

References

- [1] A. J. Ishlinsky. The axial-symmetrical problem in plasticity and the brinell test. *Theoretical Research Translation*, 2:47, 1944.
- [2] L. Y. Li, C. Y. Wu, and C. Thornton. A theoretical model for the contact of elastoplastic bodies. *Proceedings of the Institution of Mechanical Engineers, Part C: Journal of Mechanical Engineering Science*, 216(4):421–431, 2001.
- [3] F. Wang and L. M. Keer. Numerical simulation for three dimensional elastic-plastic contact with hardening behavior. *Journal of Tribology*, 127(3):494–502, 2005.
- [4] C. H. Lee and S. Kobayashi. Elastoplastic analysis of plane-strain and axisymmetric flat punch indentation by the finite-element method. *International Journal of Mechanical Sciences*, 12(4):349–370, 1970.
- [5] J. Jiang, G. B. Sinclair, and W. J. Meng. Quasi-static normal indentation of an elasto-plastic substrate by a periodic array of elastic strip punches. *International Journal of Solids and Structures*, 46(20):3677–3693, 2009.
- [6] K. Komvopoulos. Elastic-plastic finite element analysis of indented layered media. *Journal of Tribology*, 111(3):430–439, 1989.
- [7] J. Yang and K. Komvopoulos. Dynamic indentation of an elastic-plastic multi-layered medium by a rigid cylinder. *Journal of Tribology*, 126(1):18–27, 2004.
- [8] G. Karami. Boundary element analysis of two-dimensional elastoplastic contact problems. *International Journal for Numerical Methods in Engineering*, 36(2):221–235, 1993.
- [9] M. H. Aliabadi and D. Martin. Boundary element hyper-singular formulation for elastoplastic contact problems. *International Journal for Numerical Methods in Engineering*, 48(7):995–1014, 2000.
- [10] C. Oysu and R. T. Fenner. Coupled fem-bem for elastoplastic contact problems using lagrange multipliers. *Applied Mathematical Modelling*, 30(3):231–247, 2006.
- [11] B. C. Lee and B. M. Kwak. A computational method for elasto-plastic contact problems. *Computers & Structures*, 18(5):757–765, 1984.
- [12] H. W. Zhang, S. Y. He, X. S. Li, and P. Wriggers. A new algorithm for numerical solution of 3D elastoplastic contact problems with orthotropic friction law. *Computational Mechanics*, 34(1):1–14, 2004.
- [13] N. Silvestre and D. Camotim. First-order generalised beam theory for arbitrary orthotropic materials. *Thin-Walled Structures*, 40(9):755–789, 2002.

- [14] W. Yu, V. V. Volovoi, D. H. Hodges, and X. Hong. Validation of the variational asymptotic beam sectional analysis. *AIAA Journal*, 40(10):2105–2112, 2002.
- [15] J. C. Simo, P. Wriggers, K. H. Schweizerhof, and R. L. Taylor. Finite deformation post-buckling analysis involving inelasticity and contact constraints. *International Journal for Numerical Methods in Engineering*, 23(5):779–800, 1986.
- [16] P. Wriggers and G. Zavarise. On contact between three-dimensional beams undergoing large deflections. *Communications in Numerical Methods in Engineering*, 13(6):429–438, 1997.
- [17] G. Zavarise and P. Wriggers. Contact with friction between beams in 3-d space. *International Journal for Numerical Methods in Engineering*, 49(8):977–1006, 2000.
- [18] P. Litewka and P. Wriggers. Contact between 3D beams with rectangular cross-sections. *International Journal for Numerical Methods in Engineering*, 53(9):2019–2041, 2002.
- [19] E. Carrera, M. Cinefra, M. Petrolo, and E. Zappino. *Finite element analysis of structures through unified formulation*. John Wiley & Sons, 2014.
- [20] A. Pagani and E. Carrera. Unified formulation of geometrically nonlinear refined beam theories. *Mechanics of Advanced Materials and Structures*, 25(1):15–31, 2018.
- [21] M. Petrolo, M. H. Nagaraj, I. Kaleel, and E. Carrera. A global-local approach for the elastoplastic analysis of compact and thin-walled structures via refined models. *Computers & Structures*, 206:54–65, 2018.
- [22] I. Kaleel, M. Petrolo, A. M. Waas, and E. Carrera. Micromechanical progressive failure analysis of fiber-reinforced composite using refined beam models. *Journal of Applied Mechanics*, 85(2):021004, 2018.
- [23] I. Kaleel, M. Petrolo, E. Carrera, and A. M. Waas. A computationally efficient concurrent multiscale framework for the linear analysis of composite structures. *AIAA Journal*. In Press, doi:10.2514/1.J057880.
- [24] I. Kaleel, M. Petrolo, E. Carrera, and A. M. Waas. A computationally efficient concurrent multi-scale framework for the nonlinear analysis of composite structures. *AIAA Journal (accepted)*. In Press, doi:10.2514/1.J057881.
- [25] E. Carrera and M. Petrolo. Refined beam elements with only displacement variables and plate/shell capabilities. *Meccanica*, 47(3):537–556, 2012.
- [26] A.G. de Miguel, I. Kaleel, M.H. Nagaraj, A. Pagani, M. Petrolo, and E. Carrera. Accurate evaluation of failure indices of composite layered structures via various fe models. *Composites Science and Technology*, 167:174 – 189, 2018.
- [27] X. Zhang, H. Zhang, and Z. Wang. Bending collapse of square tubes with variable thickness. *International Journal of Mechanical Sciences*, 106:107–116, 2016.

- [28] C. K. Choi and G. T. Chung. A gap element for three-dimensional elasto-plastic contact problems. *Computers & Structures*, 61(6):1155–1167, 1996.